Generation of bursting magnetic fields by nonperiodic torsional flows

Juan Sánchez Umbría* and Marta Net†

Departament de Física, Universitat Politècnica de Catalunya.

Jordi Girona Salgado 1-3. Campus Nord. Mòdul B4. 08034 Barcelona. Spain

(Dated: November 20, 2019)

Abstract

A mechanism for the cyclic generation of bursts of magnetic fields by nonlinear torsional flows of complex time dependence but very simple spatial structure is described. These flows were obtained numerically as axisymmetric solutions of convection in internally heated rotating fluid spheres in the Boussinesq approximation. They behave as repeated transients, which start with nearly periodic oscillations of the velocity field of slowly increasing amplitude. This regime is followed by a chaotic fast increase and a final decrease of the amplitude of, at least, one order of magnitude. The magnetic field decays due to the magnetic diffusion during the regular oscillations, but it grows in the form of bursts during the intervals of irregular time dependence of the velocity. The magnetic field is strongly localized in spirals, with spatial- and temporal-dependent intensity.

* juan.j.sanchez@upc.edu

† marta.net@upc.edu

I. INTRODUCTION

The generation of magnetic fields by thermal convection is a fundamental subject of study in astrophysics and geophysics. Many efforts have concentrated in studying dynamos driven by thermal Rossby waves and bifurcated flows at moderate Prandtl numbers, Pr, because these waves were the stable solutions visualized experimentally and found from direct numerical simulations (DNSs) in rotating heated spheres and spherical shells (see Refs. [1–11] among many others). Most of them use the Boussinesq or anelastic approximations. These flows are axially non-symmetric and their velocity, $\boldsymbol{v}$, and temperature, T, fields are symmetric or almost symmetric by reflections with respect to the equator, i.e., they fulfill or closely fulfill $(v_r, v_\theta, v_\varphi)(r, \theta, \varphi) = (v_r, -v_\theta, v_\varphi)(r, \pi - \theta, \varphi)$ and $T(r, \theta, \varphi) = T(r, \pi - \theta, \varphi)$, θ and φ being, respectively, the colatitude and the longitude. The efficiency of these dynamos at low Reynolds number depends on the generation of mean zonal flows. The magnetic fields have, in general, a large-scale dipolar or multipolar structure like those observed in several planets. Simultaneously, other studies (see Refs. [12–19] among many others) focus on understanding the magnetic fields observed in stars, mainly in the photosphere of the Sun, and in the inter-stellar medium. These fields are associated with the turbulent motions of plasmas at high Reynolds numbers, and therefore they lack any symmetry. Their study requires adding hyperdiffusivities to the equations or the development of tailored models [20, 21]. There are several recent reviews [22–24] and books [25–28] covering the current knowledge of astrophysical and geophysical dynamos, under any point of view, i.e., focusing either on direct observations and laboratory experiments or on DNSs and theoretical models. In any case two fundamental points are to understand the transfer and dissipation of magnetic energy from large to small scales, and from the small magnetic scales to the small kinetic scales by means of reversed dynamos [19].

Large-scale dynamos driven by turbulent flows are studied through mean-field theories. They usually assume that the small scales generated by the turbulent velocity field originate in the shredding of the large magnetic field lines, and that they disappear when the mean field vanishes (see, e.g., Refs. [22, 28]). On the other hand, homogeneous and isotropic turbulence can generate directly self-sustained small-scale magnetic fields by means of random stretching and folding of the small field lines (see, e.g., [28, 29]).

Recently Sánchez *et al.* [30], Zhang *et al.* [31], and Kong *et al.* [32] found that axially

axisymmetric time-periodic flows, with prevailing equatorial antisymmetric velocity and temperature fields (torsional flows) can also be preferred at the onset of convection. At low Ekman number, Ek (defined below as the inverse of the rotation rate in viscous time units), this holds for small Pr fluids, like that of the liquid metals for which $\mathrm{Pr} \lesssim 0.1$ under different temperature and pressure conditions (see, e.g., estimations in Refs. [33–35]). The flows bifurcated from these solutions are three-dimensional, but they retain a large antisymmetric and torsional part satisfying $(v_r^a, v_\theta^a, v_\varphi^a)(r,\theta,\varphi) = (-v_r^a, v_\theta^a, -v_\varphi^a)(r,\pi-\theta,\varphi)$, and $T^a(r,\theta,\varphi) = -T^a(r,\pi-\theta,\varphi)$. Then it is important to know if the torsional velocity fields are able of driving dynamos, and if so, what is the structure of the generated magnetic fields. This paper is mainly devoted to solving a fundamental problem of magnetohydrodynamics (MHD): to find out if nearly heteroclinic cycles with these latter symmetry properties are able to generate and sustain magnetic fields by a purely kinematic action. The flows were found by DNSs as solutions of the axisymmetric Navier-Stokes equation for an internally heated rotating fluid sphere with stress-free conditions at the boundary [36].

Kinematic dynamos driven by convective flows of complex time dependence have been studied recently in Refs. [37] and [38]. Calkins *et al.* [37] focused on dynamos driven by velocity fields ranging from laminar flows to geostrophic turbulence. The flows were obtained by integrating a quasigeostrophic asymptotic model based on the anisotropic structure of the convection in a plane three-dimensional (3D) layer. They found a weak influence of the velocity field on the spatial characteristics of the large-scale magnetic field, but the behavior of the small-scale magnetic field showed important variations when the type of forcing was changed. Currie and Tobias [38] considered a convective dynamo model in a Cartesian domain, in which the shear of a two-dimensional flow is generated self-consistently by a horizontal temperature gradient and a rotation vector oblique to gravity. They found this system is a good dynamo even at high magnetic Reynolds number, for which other models pointed to a decrease of the efficiency of convection to sustain magnetic fields. However these flows act only as small-scale dynamos.

In a full MHD problem, the evolution of a magnetic field, $\boldsymbol{B}$, from a weak seed can be divided in two stages: a kinematic phase, in which there is an exponential growth of $\boldsymbol{B}$ and the Lorentz force is unimportant, and the nonlinear saturation phase, in which $\boldsymbol{B}$ is able to change the flow and stop the growth. The spatial scale of $\boldsymbol{B}$, which will depend on the parameters of the problem, is selected during the first phase, but it may change in the

second [13]. In contrast, a kinematic dynamo problem (like that studied in this article) is linear in $\boldsymbol{B}$, uncoupled from the origin of the forcing velocity field. It is in fact an eigenvalue problem for steady and periodic flows. Therefore, in spherical geometry the azimuthal wave number, m, of $\boldsymbol{B}$ can be selected in advance by expanding it in spherical harmonics. The solution provides a growth rate for any magnetic Prandtl number, $\mathrm{Pr_m}$, also fixed in advance, and the corresponding leading eigenfunction, which gives the structure of the magnetic field. In the case of periodic flows, the hydrodynamic equation must be integrated together with the induction equation, unless the time dependence is trivial (for instance if it is harmonic). The same holds for temporally chaotic or turbulent velocity fields. The information obtained is then the average growth or decay of $\boldsymbol{B}$, and its time evolution. Since the different azimuthal wave numbers are uncoupled, studying the interchange of magnetic energy between them or possible energy cascades does not make sense.

Dynamos driven by heteroclinic cycles were studied from the late 1980s mainly in plane layers [39] or even in spherical geometry [40]. In the first work, the authors showed that structurally stable heteroclinic cycles can be destabilized transversely by applying very small amounts of noise, even when the individual fixed points of the cycle are stable to transverse modes. As an example they simulated a convectively driven dynamo in a plane layer, in which the magnetic field strength acted as the transverse coordinate. The equilibrium points consisted of rolls with different symmetries, which could not lead separately to dynamo instability. However, these flows were able to increase the magnetic energy from an initial weak seed for a finite time before magnetic diffusion led to exponential decay. Gog *et al.* [39] integrated the equations adding at each time-step a normally distributed noise. They showed that the instability mechanism depended on constructive interactions between transiently growing solutions. Consequently, non-normality of the transverse dynamics favored the instability. In Refs. [40, 41] the states making up the cycle were themselves unstable to dynamo action.

In this article, the equations and their numerical treatment are discussed in Sec. II, which includes some tests to check the code of the induction equation. In Sec. III the thermal convective flows computed in rotating fluid spheres at low Pr are briefly introduced. Section IV contains the description of the bursting magnetic fields generated by kinematic dynamo action, and some tests to check the robustness of the calculations. The paper concludes in Sec. V with some remarks on the results obtained.

II. EQUATIONS AND NUMERICAL METHODS

To study a kinematic dynamo generated by complex time-dependent velocity fields, $\boldsymbol{v}$, in a fluid sphere, the induction equation

$$\partial_t \boldsymbol{B} = {\rm Pr_m}^{-1} \Delta \boldsymbol{B} + \boldsymbol{\nabla} \times (\boldsymbol{v} \times \boldsymbol{B}), \tag{1}$$

for the magnetic field $\boldsymbol{B}$ must be time evolved together with the equations that supply $\boldsymbol{v}$, responsible for the dynamo effect.

Equation (1) has been written in nondimensional form by using the radius of the sphere, r_o, as length scale and $t_\nu = r_o^2/\nu$ as timescale, ν being the kinematic viscosity. The magnetic Prandtl number is ${\rm Pr_m} = \nu/\eta$, $\eta = 1/\sigma\mu_0$ being the magnetic diffusivity. The coefficient σ is the conductivity of the fluid and μ_0 is its magnetic permeability. It represents the ratio of the magnetic to the viscous timescales, therefore the magnetic timescale is given by $t_\eta = {\rm Pr_m} t_\nu$. The critical ${\rm Pr_m}$ is the value above which the magnetic field generated by dynamo effect can be sustained. The results obtained will be shown versus the viscous time scale.

The outer space is considered a homogeneous dielectric, of permeability μ_o, extending to infinity. The boundary conditions of $\boldsymbol{B}$ between a conductor (i) and an insulator (o) are $\hat{\boldsymbol{r}} \cdot (\boldsymbol{B}^o - \boldsymbol{B}^i) = 0$, and $\hat{\boldsymbol{r}} \times (\boldsymbol{B}^o - \boldsymbol{B}^i) = 0$ if $\mu_o \approx \mu_0$. The unit vector $\hat{\boldsymbol{r}}$ is normal to the boundary of the sphere pointing outwards. Then the components of $\boldsymbol{B}$ are continuous across the boundary, $B_r^o = B_r^i$, $B_\theta^o = B_\theta^i$, $B_\varphi^o = B_\varphi^i$.

The axisymmetric velocity field, $\boldsymbol{v}$, is obtained from numerical simulations of the thermal convection of a self-gravitating ($\boldsymbol{g} = -\gamma \boldsymbol{r}$) fluid sphere, subject to internal uniform heating, with stress-free boundary conditions. The flow is inertial at low Ek, so by neglecting the Lorentz force the magnetic fields obtained will be different from those in magnetostrophic balance, being close to flows with Elsasser numbers much lower than one.

The magnetic field is split into toroidal, G, and poloidal, H, components, and treated numerically as the velocity field $\boldsymbol{v}(r,\theta,t) = \boldsymbol{\nabla} \times (\Psi(r,\theta,t)\boldsymbol{r}) + \boldsymbol{\nabla} \times \boldsymbol{\nabla} \times (\Phi(r,\theta,t)\boldsymbol{r})$ in Ref. [36], where the physical and dynamical properties of $\boldsymbol{v}$ were studied. Then

$$\boldsymbol{B}(r,\theta,\varphi,t) = \boldsymbol{\nabla} \times (G(r,\theta,\varphi,t)\boldsymbol{r}) + \boldsymbol{\nabla} \times \boldsymbol{\nabla} \times (H(r,\theta,\varphi,t)\boldsymbol{r}). \tag{2}$$

The magnetic potentials are expanded in spherical harmonic series. Since Eq. (1) is linear, the problem decouples for the azimuthal order. Therefore the expansion for a fixed order,

m, up to degree L is

$$X(r,\theta,\varphi,t) = \sum_{l=m}^{L} X_l^m(r,t) P_l^m(\cos\theta)\exp(im\varphi), \tag{3}$$

where $X = (G, H)$, and $P_l^m(\cos\theta)$ are the normalized associated Legendre functions defined as

$$P_l^m(\cos\theta) = \sqrt{\frac{2l+1}{2}\frac{(l-m)!}{(l+m)!}}\,\tilde{P}_l^m(\cos\theta), \quad \text{for} \quad l \geq 0, \text{ and } 0 \leq m \leq l, \tag{4}$$

where $\tilde{P}_l^m(\cos\theta)$ are the standard Legendre functions. Finally, collocation in a radial Gauss-Lobatto mesh of N_r points is used. Then Eq. (1) splits into the scalar equations

$$(\partial_t - {\rm Pr_m}^{-1}\Delta)\mathscr{L}_2 G = \boldsymbol{r}\cdot\boldsymbol{\nabla}\times\boldsymbol{\nabla}\times(\boldsymbol{v}\times\boldsymbol{B}) \tag{5}$$

$$(\partial_t - {\rm Pr_m}^{-1}\Delta)\mathscr{L}_2 H = \boldsymbol{r}\cdot\boldsymbol{\nabla}\times(\boldsymbol{v}\times\boldsymbol{B}). \tag{6}$$

The boundary conditions of $\boldsymbol{B}$ at $r = r_o$ become

$$G_l^m = 0 \qquad \text{and} \qquad \frac{l+1}{r_o}H_l^m + \frac{dH_l^m}{dr} = 0, \tag{7}$$

in terms of the amplitudes of the potentials. At $r = 0$ only regularity conditions are required.

The linearity of Eq. (1) for the kinematic dynamo has several implications. When the forcing velocity field is axisymmetric, as is the case of this article, Eq. (1) can be separated, as stated in the introduction, into a system of uncoupled equations, one for each azimuthal wave number m. They can therefore be studied separately. It also implies that $\boldsymbol{B}$ does not saturate. Its norm can, on average, grow or decay exponentially. Consequently, an interpolation method is used here to approximate the critical parameter for the generation of magnetic fields by complex time-dependent flows. The parameters of nearby solutions, of increasing and decreasing growth rates obtained by time evolution, allow us to determine an approximation of the critical value, and the structure of the most unstable eigenfunction.

The velocity field, $\boldsymbol{v}$, is calculated by integrating the Boussinesq approximation of the Navier-Stokes and energy equations, written in terms of the potentials Ψ and Φ,

$$(\partial_t - \Delta)\,\mathscr{L}_2\Psi = -2{\rm Ek}^{-1}\mathscr{Q}\Phi - \boldsymbol{r}\cdot\boldsymbol{\nabla}\times(\boldsymbol{\omega}\times\boldsymbol{v}), \tag{8}$$

$$(\partial_t - \Delta)\,\mathscr{L}_2\Delta\Phi = 2{\rm Ek}^{-1}\mathscr{Q}\Psi - \mathscr{L}_2\Theta + \boldsymbol{r}\cdot\boldsymbol{\nabla}\times\boldsymbol{\nabla}\times(\boldsymbol{\omega}\times\boldsymbol{v}), \tag{9}$$

$$({\rm Pr}\partial_t - \Delta)\,\Theta = {\rm Ra}\mathscr{L}_2\Phi - {\rm Pr}(\boldsymbol{v}\cdot\boldsymbol{\nabla}\Theta), \tag{10}$$

together with the induction equation.

In Eqs. (8)-(10) and (5) and (6) the operator $\mathscr{L}_2$ is defined as $\mathscr{L}_2 = -r^2\Delta + \partial_r(r^2\partial_r)$, and $\mathscr{Q}$ as $\mathscr{Q} = r\cos\theta\Delta - (\mathscr{L}_2 + r\partial_r)(\cos\theta\partial_r - r^{-1}\sin\theta\partial_\theta)$ in Eqs. (8) and (9). Moreover, $\boldsymbol{\omega} = \boldsymbol{\nabla}\times\boldsymbol{v}$ is the vorticity, and $\Theta(r,\theta) = T(r,\theta) - T_c(r)$ is the temperature perturbation from the conduction state, $T_c(r)$, in $\nu^2\gamma\alpha r_o^4$ units

The nondimensional parameters of the convective system are the Rayleigh, Prandtl, and Ekman numbers, defined as

$$\mathrm{Ra} = \frac{S\gamma\alpha r_o^6}{3\kappa^2\nu}, \qquad \mathrm{Pr} = \frac{\nu}{\kappa} \quad \text{and} \qquad \mathrm{Ek} = \frac{\nu}{\Omega r_o^2}, \tag{11}$$

respectively. The coefficient κ is the thermal diffusivity, α the thermal expansion coefficient, Ω the angular velocity, and S accounts for the internal heat generation. It appears in Eq. (10) in the term $\mathrm{Ra}\mathscr{L}_2\Phi$ through the Rayleigh number.

The stress-free and perfectly conducting boundary conditions become

$$\Phi = \partial_{rr}^2\Phi = \partial_r(\Psi/r) = \Theta = 0 \quad \mathrm{a}t \quad r = r_o. \tag{12}$$

Since stress-free boundary conditions are applied, the conservation of the z component of the angular momentum is achieved in the way explained in Sánchez Umbría and Net [36]. At $r = 0$ only regularity conditions are required.

The functions Φ, Ψ, and Θ are expanded in spherical harmonic series of order 0 and degree up to L as

$$Z(r,\theta,t) = \sum_{l=0}^{L} Z_l^0(r,t)P_l^0(\cos\theta),$$

where $Z = (\Phi,\Psi,\Theta)$. The indeterminacy of Φ and Ψ is solved by taking $\Phi_0^0 = \Psi_0^0 = 0$.

In order to check the new time integration code for the system (5)-(6) with boundary conditions (7) using a radial pseudo-spectral method, the steady axisymmetric velocity field

$$\boldsymbol{u}(r,\theta) = \boldsymbol{\nabla}\times(t_1^0(r)Y_1^0(\theta)\,\hat{r}) + \boldsymbol{\nabla}\times\boldsymbol{\nabla}\times(\varepsilon s_1^0(r)Y_1^0(\theta)\,\hat{r}), \tag{13}$$

with $t_1^0(r) = s_1^0(r) = r\sin(\pi r)$ and $\varepsilon = 0.17$, proposed by Dudley and James (DJ) [42], was used. This field was modified to take into account our different decomposition of the velocity in toroidal and poloidal components, and the different normalization of the Legendre polynomials. Specifically, $t_1^0(r) = s_1^0(r) = \sqrt{2/3}\sin(\pi r)$ were defined because we have an extra factor r in the definition of $\boldsymbol{B}$ (see Eq. (2)), and the different normalization introduces

the factor $\sqrt{(2l+1)/2}$. Then $(Y_l^m)_{SN}(\theta,\varphi) = \sqrt{(2l+1)/2}(Y_l^m)_{DJ}(\theta,\varphi)$. Moreover, due to the different scales taken by the authors, the relation between our magnetic Prandtl number and their magnetic Reynolds number is $\mathrm{Pr_m^{SN}} = \mathrm{Re_m^{DJ}}$, and that between the timescales is $t_{SN} = \mathrm{Pr_m} t_{DJ}$, which gives the relation between the eigenvalues of the problem $\lambda_{SN} = \mathrm{Pr_m^{-1}}\lambda_{DJ}$. The resulting velocity field $\boldsymbol{u}(\boldsymbol{r})$ consists of a single vortex, symmetric with respect to the equator. The same field was also used by Li *et al.* [43] to test their very accurate Galerkin scheme to solve the kinematic dynamo problem in a full sphere. They got as leading eigenvalue, in DJ units, $(\lambda_r, \lambda_i) = (0.313151589, 34.843592723)$, for $m = 1$, $\mathrm{Re_m^{DJ}} = 160$, and $N = L = 35$, N being the number radial functions of their approximation. In our case, the leading eigenvalues of Eq. (1), for the same steady field and parameter $\mathrm{Pr_m} = 160$, were calculated from the multipliers of the map $\boldsymbol{B} \to \varphi(\tau, \boldsymbol{v}, p)\boldsymbol{B}$ by using the ARPACK package based on Arnoldi algorithm [44], $\varphi(\tau, \boldsymbol{v}, p)$ being the flow of Eq. (1) at a fixed time τ, $\boldsymbol{v}$ the DJ velocity field, and $p = \mathrm{Pr_m}$ (see Ref. [45] for more details).

Several of the time integrators compared in Ref. [46], for the pure hydrodynamic problem, were tested for the integration of the coupled system of Eqs. (5), (6), (8)-(10). It turned out that the subroutine DLSODPK of the ODEPACK package [47] was the most efficient, because there are very different timescales in the problem. It is a fully implicit variable step size and variable order (VSVO) method, based on backward differentiation formulas (BDF) of orders up to six. This means to control simultaneously the order and the time step to keep the local error of the integration below a given tolerance, using the largest possible time step.

Tests were done for several truncation numbers N_r and L. An initial condition was first obtained by integrating the induction equation, from a random seed, the time needed to filter the fast decaying modes. Then Arnoldi's iterations were started using an integration time $\tau = 0.1$ for the map $\varphi(\tau, \boldsymbol{v}, p)$. The results (taking into account the different normalization of the spherical harmonics and scales) agree very well with those of Ref. [43] even with the lower resolution used, with negligible differences between them. For instance, with $N_r = L = 35$, $(\lambda_r, \lambda_i) = (0.31315335, 34.84359343)$ was obtained.

Following the same method we have solved the eigenvalue problem for the time-periodic axisymmetric solutions of Eqs. (8)-(10) with boundary conditions (12). We have been unable to find a self-sustained $\boldsymbol{B}$ driven by pure periodic torsional oscillations. When $\mathrm{Pr_m}$ is increased the modulus of the leading Floquet multiplier tends to 1, never reaching this

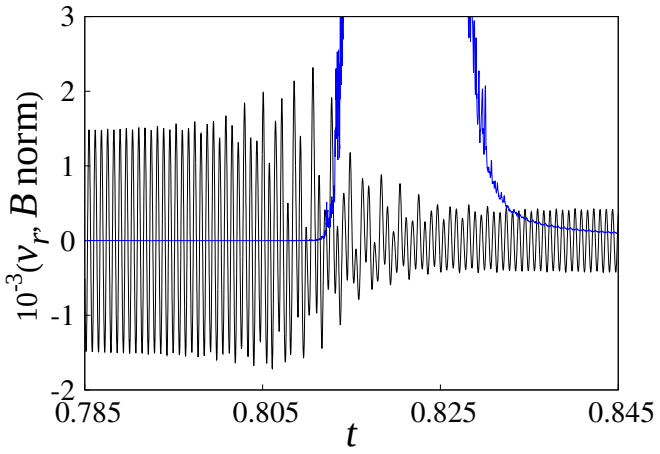

FIG. 1. Radial component of the velocity at a point of the sphere (oscillatory curve, black online) and norm of the magnetic field (curve with the fast growth at $t = 0.810$, blue online) showing the timescale of the temporally chaotic motion. The parameters are $\mathrm{Ek} = 10^{-4}$, $\mathrm{Pr} = 10^{-3}$, $\mathrm{Ra} = 10^4$ and $\mathrm{Pr_m} = 75$.

value. As will be seen in the next section the periodic orbits play the role of the equilibria in Ref. [39].

III. THE VELOCITY FIELDS

The velocity and magnetic fields were calculated by discretizing Eqs. (5), (6) and (8-10), together with boundary conditions (12) and (7), with a maximum resolution of $N_r \times L = 150 \times 80$ in order to confirm the validity of the results. This corresponds to $N_\theta = 124$ points in colatitude because aliasing is removed in this coordinate (see Ref. [48]). The finer meshes are only needed to resolve the smallest spatial scales of the magnetic field. The velocity field is smoother and can be represented with lower resolutions. The next section includes a test with different resolutions for the magnetic field in a temporally chaotic regime.

Two velocity fields of different and complex time dependence are used in the study. Both are temporally chaotic, and correspond, respectively, to $\mathrm{Pr} = 10^{-3}$, $\mathrm{Ek} = 10^{-4}$ and $\mathrm{Ra} = 10000$, and $\mathrm{Pr} = 10^{-2}$, $\mathrm{Ek} = 10^{-3}$ and $\mathrm{Ra} = 21250$. These low Prandtl numbers have been selected because they fulfill the relation $\mathrm{Pr/E} \approx 10$ that, according to [31], guarantees the existence of flows with a dominant antisymmetric component with respect to the equator,

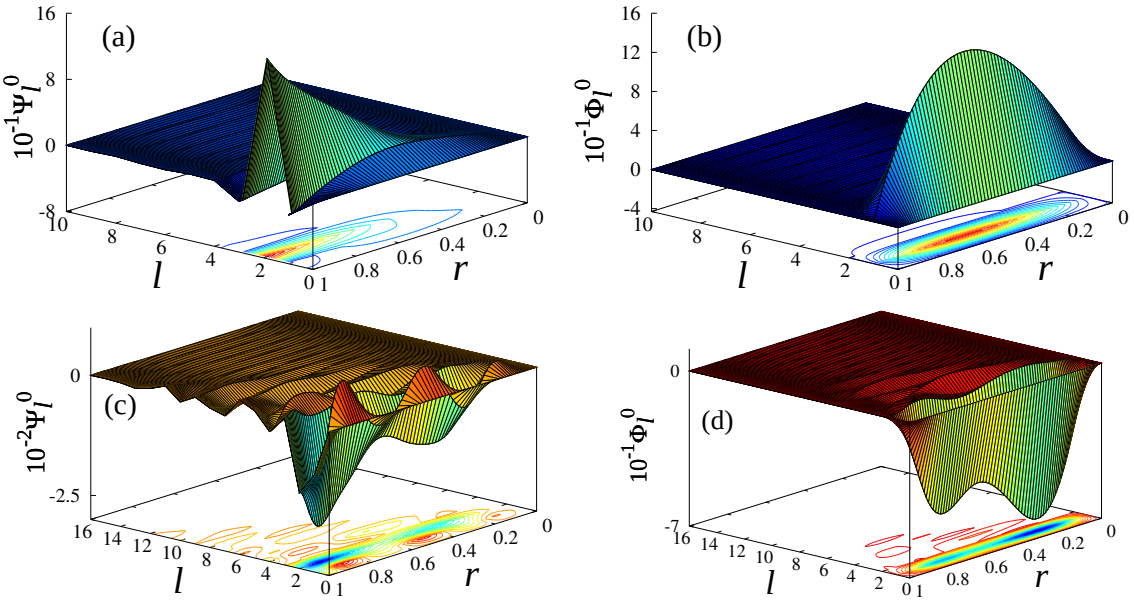

FIG. 2. Potentials of the velocity field [(a), (b)] at $t = 1.071$ during the regular oscillations, and [(c), (d)] at $t = 1.2836$ during the irregular motion. The parameters are $\mathrm{Ek} = 10^{-4}$, $\mathrm{Pr} = 10^{-3}$, $\mathrm{Ra} = 10^4$, and $\mathrm{Pr_m} = 62$. The times indicated correspond to Fig. 3(c).

and approximate the hydrodynamic Prandtl number of liquid metals and solar plasmas [35].

The velocity fields of the solutions corresponding to $\mathrm{Pr} = 10^{-3}$ and $\mathrm{Ek} = 10^{-4}$ behave as repeated transients, which start with nearly periodic oscillations of the velocity field of slow increasing amplitude. This regime is followed by a chaotic fast increase and decrease of the amplitude. The frequency of the transients corresponds to the frequency appearing at the third Hopf bifurcation of the flow from the conduction state, when the axisymmetry is kept. This behavior was identified in Sánchez Umbría and Net [36] as a global dynamics in which the trajectories remain for a long time close to the unstable manifold of a periodic orbit, which is close to the stable manifold of another more unstable cycle. When the trajectories approach the second orbit they are repelled along its unstable manifold, and they are sent back quickly to the vicinity of the first periodic orbit, moving close to what it is known as a heteroclinic cycle [see Figs. 13(a) and 13(b) in Ref. [36] to visualize this dynamics]. The plots of v and Θ in the $\theta - \varphi$, $r - \varphi$ and $r - \theta$ sections look like those of the periodic solutions shown for instance in Fig. 5 of Ref. [36], during the normal oscillations. They look irregular during the chaotic motion, with increasing and decreasing intensity. When the norm of $\boldsymbol{v}$

increases, the flow intensifies mainly near the axis. Animations of this dynamics can be seen in the Supplemental Material [49] for this paper.

The first animation illustrates the variation of the velocity field and the temperature perturbation during the chaotic motion, in the sections indicated by dashed lines. The parameters are those of Fig. 1, and the time interval, (0.801, 0.816), is contained in that shown there. It includes an initial part in which the amplitude of the oscillations is still growing, followed by an irregular increase and decay (see the time in the movie). The length of the arrows and the intensity of the color are scaled with respect to the maximum over the full sphere and over the time interval considered, to allow seeing the growth and decay of $\boldsymbol{v}$. In the second animation the contour plots correspond to the kinetic energy density. In this case, the intensity of the color is scaled at each snapshot taking the maximum only over the full sphere. Therefore red corresponds to the maximal kinetic energy at each time instant. In this way it is easier to see where are the maxima. Both animations show that during the chaotic motion the spatial scale of the structures is still large.

Figures 2(a) and 2(b) show that when the trajectory remains on the unstable manifold of the first periodic orbit the velocity potentials can be described with just three associated Legendre functions, P_1^0, P_2^0 and P_3^0, while in the short fast transient up to fifteen functions must be taken into account [Figs. 2(c) and 2(d)]. In the first case the kinetic energy of the fluid is concentrated close to the surface of the fluid sphere, while in the second it moves to the poles and to the center.

The second velocity field considered corresponds to a temporally chaotic flow at Ra = 21250. It appears after three Hopf bifurcations from the conduction state (see also Ref. [36]). In contrast to the preceding case this sequence of bifurcations does not lead to a global heteroclinic dynamics. The maximum value of the norm of this solution of system (8-10) has a strong variation (around 33%). The velocity field must be described by several Legendre polynomials at any time instant [as happens in the case illustrated with Figs. 2(c) and 2(d)], and the kinetic energy is always concentrated near the rotation axis and the center of the sphere (see [36] for more details).

IV. THE MAGNETIC FIELDS

Figure 3 shows the influence of the dynamics of the chaotic flows found at $\mathrm{Ek} = 10^{-4}$ and $\mathrm{Ra} = 10^4$ on the kinematic generation of $\boldsymbol{B}$. According to Refs. [50, 51], among others, the growth rate of the $m = 1$ azimuthal mode is the first in becoming positive as $\mathrm{Pr_m}$ is increased, so, after checking this point in a few cases, expansion (3) was restricted to $m = 1$ in the calculations. The left axis label denotes the Euclidean norm of the potentials of $\boldsymbol{B}$, defined as

$$\|B\|_2 = \left[\sum_{l=m}^{L} \left[\|G_l^m\|_2^2 + \|H_l^m\|_2^2 \right] \right]^{1/2}, \tag{14}$$

which, in principle, depends on the grid. The number of radial points taken to compute the figures showing norms was always the same, and the amplitudes of the Legendre polynomials of highest degree, l, were always negligible in the cases explored, either for $\boldsymbol{B}$ or $\boldsymbol{v}$. Moreover Eq. (1) is linear in $\boldsymbol{B}$, and therefore only the relative values of the amplitudes of $\boldsymbol{B}$ in Fig. 3 make sense. The right axis label indicates the scale of the radial component of $\boldsymbol{v}$, in this way the lower curve of Fig. 3(a) shows the variations of the amplitude of the flow.

The upper curve of Fig. 3(a), and those of Figs. 3(b)–3(d) represent, in logarithmic scale, the bursting magnetic field generated by the torsional chaotic flow. The first corresponds to $\mathrm{Pr_m} = 150$, far from the critical value. The bursts are extremely vigorous. The norm of $\boldsymbol{B}$ increases several orders of magnitude, and the magnetic diffusion is unable to dissipate, during the long time interval of small-amplitude oscillations between bursts, all the energy injected by the velocity field during the bursts. In this way after each burst the intensity of $\boldsymbol{B}$ is higher, as happens, for instance, in Figs. 3(a) and 3(b). Between bursts the oscillations are nearly periodic with the frequency of the periodic torsional solutions, i.e., of order Ek. When $\mathrm{Pr_m}$ is decreased the bursting phenomenon continues, but for values under the critical, the magnetic dissipation is able to reduce the magnetic field until its extinction [see Fig. 3(d)]. However, some estimations show that even in this case the complete annihilation of $\boldsymbol{B}$ could take millions of years for astrophysical objects. For a value near the critical there is a time-averaged balance (from burst to burst) between the magnetic energy dissipated and that supplied by $\boldsymbol{v}$. Then, after a burst, $\boldsymbol{B}$ nearly recovers the mean amplitude it had before, as can be seen approximately in Fig. 3(c), calculated for a value very near the critical. In this case the transient until reaching the monotonous regime takes a long time because of the

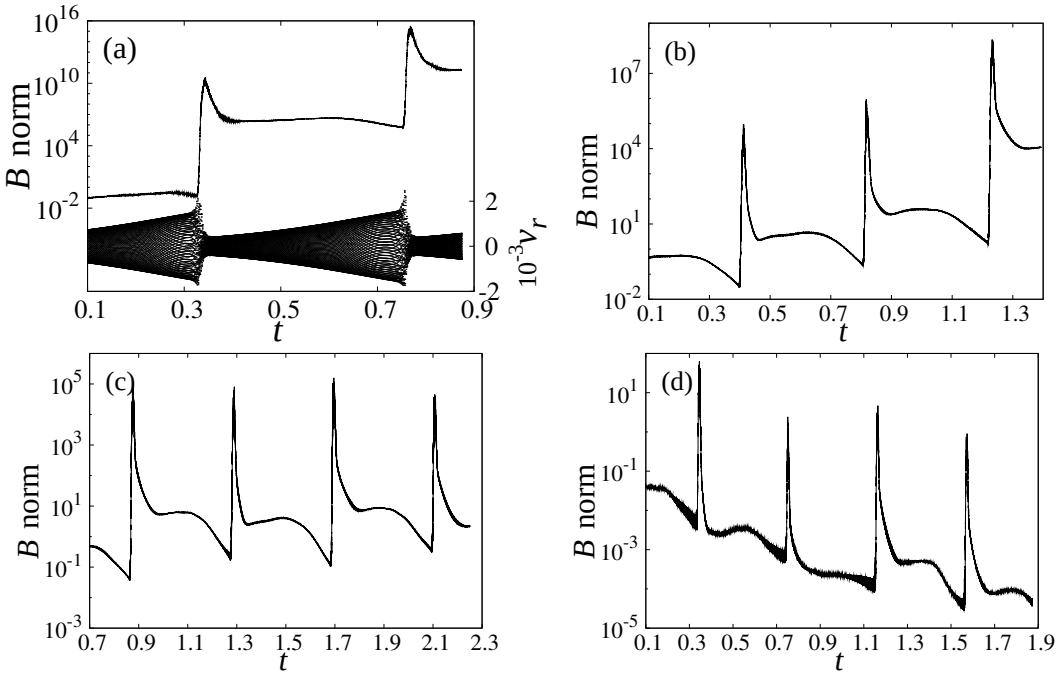

FIG. 3. (a-d) Time evolution of the l_2-norm of the potentials of the magnetic field for $\mathrm{Pr_m} = 150, 75, 62, 50$ in logarithmic scale. In (a) also time evolution of $v_r(r_o/3, \pi/6, \varphi)$ (right axis). The other parameters are $\mathrm{Ek} = 10^{-4}$, $\mathrm{Pr} = 10^{-3}$ and $\mathrm{Ra} = 10^4$.

proximity to the bifurcation.

Although it can seem from Fig. 3 that the jumps are quite abrupt, a meticulous inspection of the time evolution shows that there are very short time-scale fluctuations. Figure 4 contains some details of Fig. 3(b) in several time intervals. The first, Fig. 4(a), displays the regular oscillations between two bursts. The period of these oscillations is that of the forcing velocity, 7×10^{-4} viscous units. During this regime the time step taken by DLSODPK is of the order of 5×10^{-7}. However, in order to save storage space, the results of the time integration are written only every 6×10^{-6} time units. This means that the oscillations are smoother than what is seen in Fig. 4. The second plot is a blowup of the third burst, showing that it spans about 0.02 time units. In this case the time step is shorter, of the order of 2×10^{-7} time units. Figures 4(d) and 4(e) are details of the same burst when $\boldsymbol{B}$ increases, and when it reaches the maximum value. They illustrate that the averaged timescale of the fluctuations of the magnetic field is below 10^{-4}. Figures 4(c) and 4(f) show the loss and the gain of regularity of the oscillations at the beginning and at the end of the

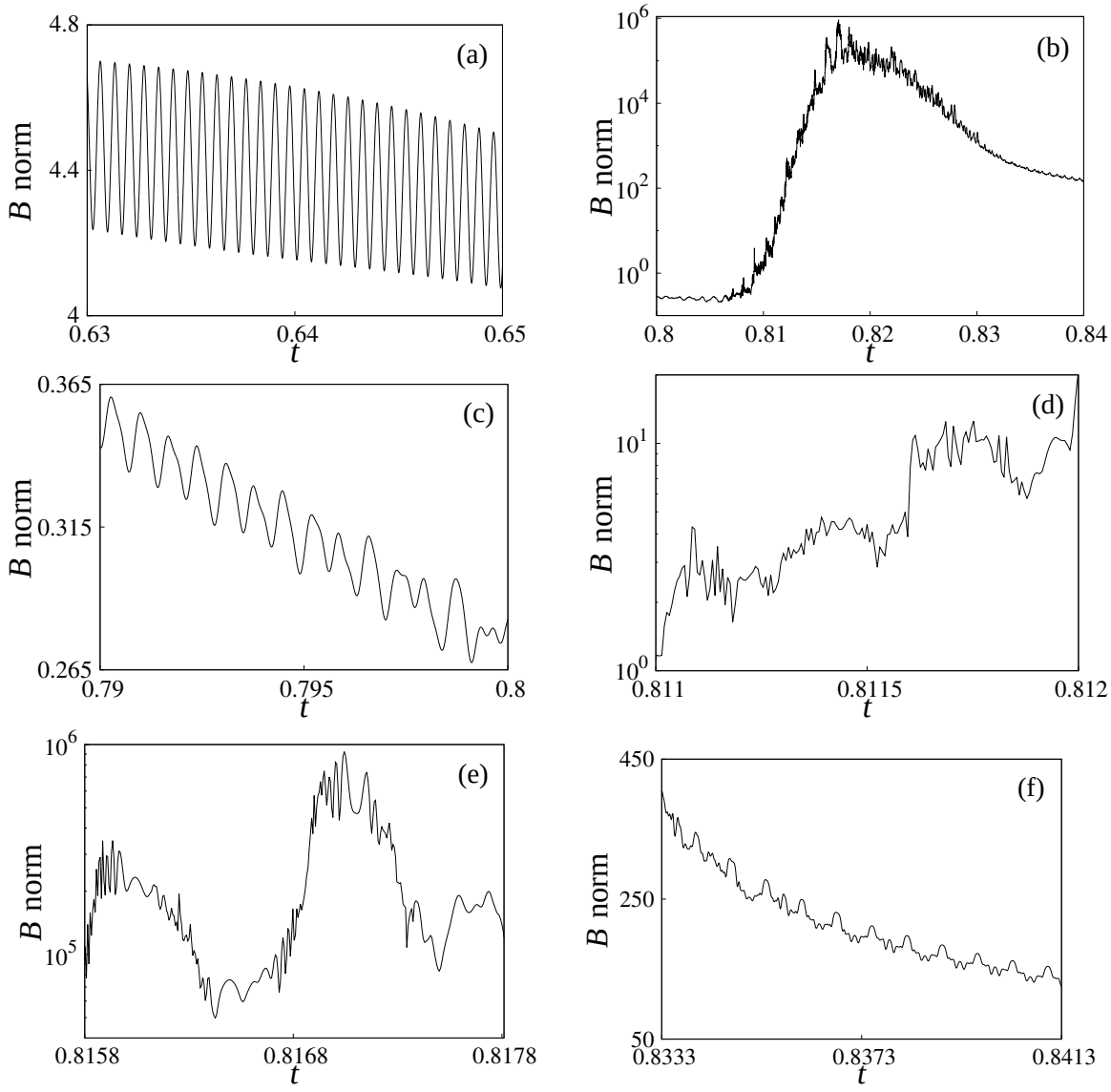

FIG. 4. (a-f) Details of Fig. 3(b). Panels (a), (c), and (f) are plotted in linear scale.

burst, respectively.

The magnetic field $\boldsymbol{B}$ was initially calculated with $N_r \times L = 60\times60$, 100×50 and 150×80, and different values of the parameters, to select an adequate discretization. Figure 5 shows three simulations for $\mathrm{Ra} = 10^4$ and $\mathrm{Pr_m} = 75$. They were started from different initial conditions with random $\boldsymbol{B}$ to check that the dynamics found is robust. The temporal sequences in Fig. 5 were shifted in time and scaled vertically to a similar level at $t = 0.4$, i.e., at the beginning of the first burst, to facilitate the comparison. In addition, the initial transients were removed. This can be done because the induction equation is linear and

there is always an undetermined multiplicative factor on $\boldsymbol{B}$.

The dynamics including the bursts is chaotic. Changes in the initial conditions give rise to different trajectories which separate exponentially. The same holds when comparing solutions corresponding to different truncation parameters, even if the initial conditions are interpolated from the same solution. Therefore it is not possible to make a complete quantitative numerical study of the convergence of the solutions with the resolution in this regime. Since it is chaotic the width, height, and fluctuations of the bursts, and the relative jump between consecutive plateaus away from the bursts, change, even for a same trajectory. In any case it was checked that, for any of the three resolutions, the time distance between bursts, T_2, is given by the period of the repeated transients of the velocity field, and that the period of the almost regular oscillations between bursts is that of the forcing, i.e., that of the inertial oscillations, T_1. These magnitudes are independent of the truncation (from a threshold of the resolution) because they depend on the regular oscillations of the velocity field, while the trajectories are spiraling close to the unstable manifold of one of the periodic orbits driving the dynamics. In contrast the shape of the bursts depends on the chaotic part of the trajectory of the velocity field outside the mentioned manifold, and they can differ from one resolution to another.

Table I summarizes an approximate quantification of the results. They agree quite well, but the width of the bursts, W_B, defined as the time distance from their starting point to the beginning of the regularization of the oscillations, is wider for the lower resolution than for the others. For this reason, since T_1 and T_2 are approximately the same for the higher resolutions, and in order to save computational time, $N_r \times L = 100 \times 50$, with $N_\theta = 76$, was usually used in the computations.

Figure 6 shows the contour plots of the largest component of $\boldsymbol{B}$, B_φ, on a spherical surface, the equatorial plane, and a meridional section, at different times. The location of the sections is indicated in the pictures, and the gray scale (color online) is normalized over the full sphere for each snapshot (group of three plots). The sections in the first and third columns pass through the maximum value of B_φ, so the radius of the spherical section is different at each t. The arrows are the projections of $\boldsymbol{B}$ on each surface. The spatial structure of $\boldsymbol{B}$ is much more complicated than that of $\boldsymbol{v}$. In this case many spherical harmonics contribute to the solution even during the transients between bursts. The components of $\boldsymbol{B}$ spiral from the interior of the sphere to its surface with variable intensity, giving rise to bands of nonzero

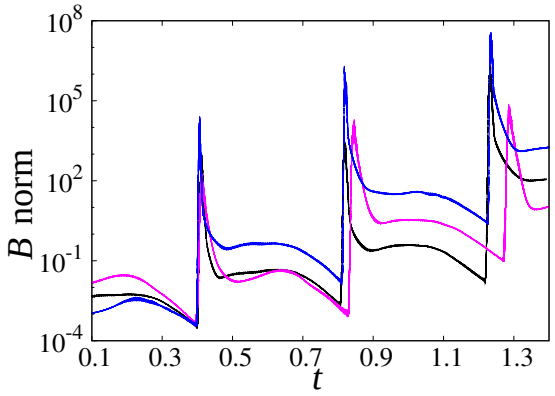

FIG. 5. Time sequences for the resolutions $N_r \times L = 60 \times 60$ (middle curve at $t = 1.1$, magenta online), 100×50 (lower curve at $t = 1.1$, black online) and 150×80 (upper curve at $t = 1.1$, blue online) for $\mathrm{Ek} = 10^{-4}$, $\mathrm{Pr} = 10^{-3}$, $\mathrm{Ra} = 10^4$, and $\mathrm{Pr_m} = 75$.

$N_r \times L$	N_θ	$10^{-4}\, T_1$	T_2	W_B	W_o
60×60	92	7.14	0.44	0.08	$\ll 10^{-4}$
100×50	76	7.14	0.41	0.023	$\ll 10^{-4}$
150×80	124	7.14	0.41	0.017	$\ll 10^{-4}$

TABLE I. Comparison of the timescales of $\boldsymbol{B}$ for different resolutions. T_1 is the period of the regular oscillations, T_2 the period of the bursts, W_B the width of the bursts in time units and W_o an approximation of the timescale of the fast fluctuations during the bursts. The parameters are $\mathrm{Pr} = 10^{-3}$, $\mathrm{Ek} = 10^{-4}$, $\mathrm{Pr_m} = 75$, and $\mathrm{Ra} = 10^4$.

$\boldsymbol{B}$ at different constant radii. In a colatitudinal section, and during the oscillations between bursts, the bands behave as very localized spots, most of the time concentrated near the outer surface at different latitudes, as in Figs. 6(a)–6(c) and Figs. 6(p)–6(r). Their position has a strong variation over time and between bursts, and can give rise to hemispherical magnetic fields in agreement with Ref. [52]. Preceding each burst these spots move towards the polar regions [see Fig. 6(d)–6(f)], and during the eruption they concentrate around the rotation axis and close to the center of the sphere. [see Figs. 6(g)–6(i) and Figs. 6(j)–6(l)].

In order to compare the above magnetic fields with those generated by the flows that appear after a sequence of Hopf bifurcations giving rise to local dynamics, the temporally chaotic $\boldsymbol{v}$ shown in the lower plot of Fig. 7 was considered. The time evolution of the

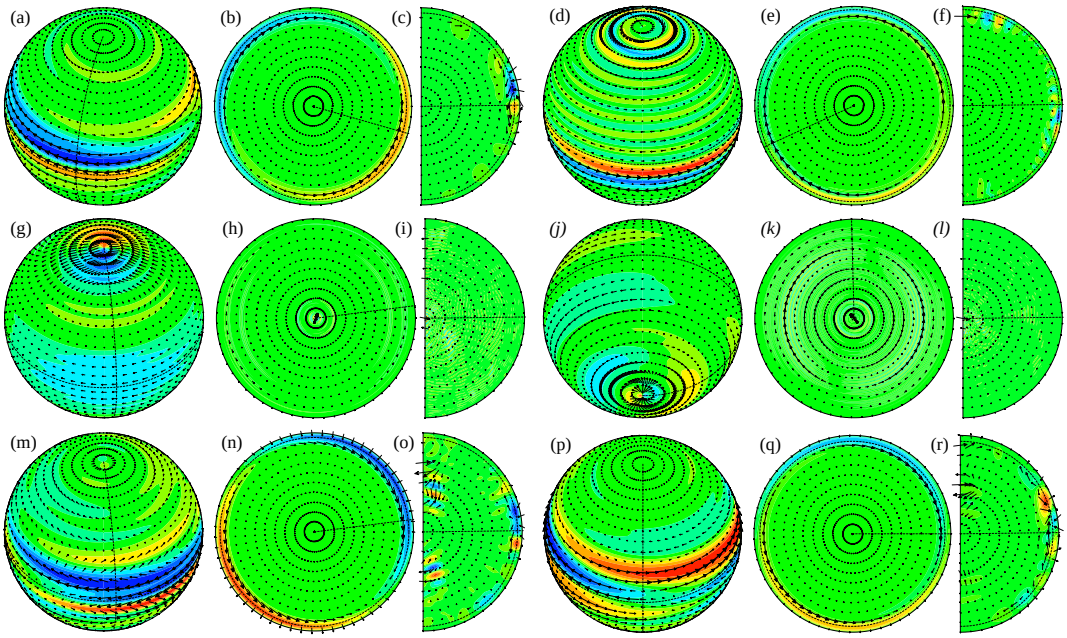

FIG. 6. Contour plots of B_φ on a spherical surface taken at $r > 0.9$ in (a), (d), (m), and (p), and at $r = 0.02$ in (g) and (f). Equatorial sections in the second column, and meridional planes in the third, indicated by dashed lines. In (a)-(c) $t = 1.4746$, (d)-(f) $t = 1.6741$, (g)-(i) $t = 1.6873$, (j)-(l) $t = 1.6947$, (m)-(o) $t = 1.7925$, and (p)-(r) 1.8697. The arrows are the projections of $\boldsymbol{B}$ on each section. The parameters are $\mathrm{Ek} = 10^{-4}$, $\mathrm{Pr} = 10^{-3}$, $\mathrm{Ra} = 10^4$, and $\mathrm{Pr_m} = 62$.

norm of $\boldsymbol{B}$, after removing the initial transient, is shown in the upper part in logarithmic scale. The magnetic Prandtl number is 27. The almost horizontal line is the exponential fit $\|\boldsymbol{B}\| = 2.34\exp(-0.19t)$, indicating that $\mathrm{Pr_m}$ is only slightly below the critical value. In fact, $\mathrm{Pr_m} = 28$ already gives a positive growth rate. Once again, the generation of magnetic field is correlated with the increase of the amplitude of the oscillations of $\boldsymbol{v}$, but the flow never reaches a regime of almost periodic oscillations, in which there is a clear decay of $\boldsymbol{B}$ due to their regularity. The structure of the magnetic field is also very localized, like that shown in the contour plots of Figs. 6, spiraling from the interior to the surface and forming thin bands on the spherical projections. The main difference is that the density of the spots in the meridional sections near the rotation axis and the interior of the sphere is significant at any time.

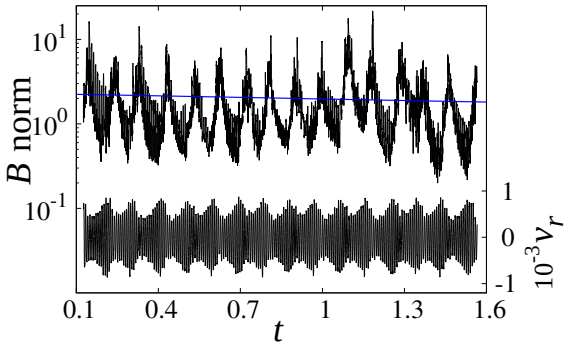

FIG. 7. Time evolution of the l_2-norm of the potentials of the magnetic field for $\mathrm{Pr_m} = 27$. The other parameters are $E = 10^{-3}$, $\mathrm{Pr} = 0.01$ and $\mathrm{Ra} = 21250$. The horizontal line (blue online) is the exponential fit of the solution.

V. DISCUSSION AND CONCLUSIONS

This work is close to those presented at the beginning of the introduction in the sense that it studies convection-driven kinematic dynamos with large-scale velocity fields obtained through DNSs, but at very low Pr and with predominantly equatorial antisymmetric oscillatory flows. Moreover, these torsional velocity fields need to develop a mean flow to generate magnetic fields, as happens in the case of the large-scale thermal waves. However in this case the simulations show that the long-sustained spiral field in the outer surface between bursts comes from the stretching of the strong $\boldsymbol{B}$ confined in the interior of the sphere during the bursts. In this way the initial small azimuthal scale of $\boldsymbol{B}$ elongates, retaining a small latitudinal scale.

In agreement with Ref. [53], it has been found that periodic axisymmetric torsional velocity fields are unable to sustain magnetic fields. The asymptotic theory of Zhang *et al.* [31] shows that periodic torsional convection is dominated at first order by inertial periodic oscillations, while buoyancy forces appear only at next order to overcome the viscous dissipation. These flows cannot generate mean flow since the Reynolds stresses related to them are zero. On the other hand, the theory of Herreman and Lesaffre [53] shows that simple inertial waves cannot drive dynamos at leading order because the *Stokes drift*, which acts as a mean flow, is zero. Moreover, one of the applications studied there is the inertial flow in a rotating sphere. Consequently, the above numerical results seem to confirm that this theory could be applied to the pure periodic case and during the long transients between bursts,

but not when the trajectory leaves the manifold connecting the unstable periodic solutions. Torsional flows, like that of Fig. 3(a), can be seen as a perturbation of the thermal-inertial solutions throughout the long time of regular oscillations. In this case they are very well represented by three Legendre functions without generation of mean flow, and $\boldsymbol{B}$ tends to decay. However, out of the manifold connecting the unstable orbits, the temporal dependence of $\boldsymbol{v}$, illustrated in Fig. 3(a), involves several Legendre functions [see Figs. 2(b) and 2(c)], generating mean flow and consequently magnetic field.

Although it is already known that the periodic torsional solutions bifurcate to 3D flows, our recent calculations show that the transition can take place through a bifurcation that breaks the axisymmetric invariance and leads the flow to drift azimuthally, as it is well known that that happens when the axisymmetry of a steady flows is broken (see, e.g., Ref. [54]). Then the quasiperiodic flow consists of a torsional dynamics precessing azimuthally. Subsequent Hopf bifurcations could either give rise to a global dynamics similar to that described in Ref. [36] with a superposed drift, or to a sequence of local bifurcations, in any case generating mean zonal flow and maintaining the torsional oscillations. However, an important open problem is to find out in a next step how the Lorentz force and the saturation of the magnetic field would affect the bursting phenomenon and the structure of $\boldsymbol{B}$. One should expect that during the bursts the balance of forces of the momentum equation will be modified. Cattaneo and Tobias [15] studied how dynamos saturate from a full MHD system (rotating plane layer) and from a turbulent shell model. Two magnetic fields were considered: one, $\boldsymbol{B}_1$, coupled with the velocity via the Lorentz term, and another, $\boldsymbol{B}_2$ uncoupled. They concluded that a saturated velocity satisfying the full MHD system, remains a source of kinematic dynamos for any initial condition of $\boldsymbol{B}_2$ not aligned with $\boldsymbol{B}_1$. Livermore *et al.* [55] analyzed the differences between a kinematic and a dynamic dynamo driven by a nonaxisymmetric helical flow in spherical geometry without rotation. They found that the nonlinear interactions enlarge the scale of $\boldsymbol{B}$ generating a significant mean component. The forcing of the kinematic dynamo studied in the present work is a predominant equatorial antisymmetric inertial flow and requires further attention. On the other hand, the unlikely preferred instability of higher azimuthal wave-number modes in some regions of the parameter space would not change the conclusions of this work. It would only lower the critical value at which the instability takes place, and it would increase the number of arms of the spirals of $\boldsymbol{B}$.

The dynamics found in this study shows two important differences with the study of Gog *et al.* [39] mentioned in the introduction, aside from the existence of rotation in our model. The states organizing the nearly heteroclinic cycle are unstable periodic orbits, and no noise is added to the system to sustain the dynamo. An initial perturbation of the zero magnetic field is enough to drive the kinematic dynamo, above the critical parameter. Although the parameters of this work are far from astrophysical and geophysical values, the velocity fields taken into account are real solutions of a thermal convection problem in internally heated rotating fluid spheres. Then the cyclic generation of $\boldsymbol{B}$ in the form of bursts, each one followed by a long interval of almost constant energy and a subsequent decay, can provide some insight for the development of theoretical models explaining observations of cyclic phenomena. The periodicity should depend on the time spent by the trajectories spiraling close to the manifold that connects the periodic orbits. The duration and height of the bursts should depend on the time spent by the trajectory outside this manifold and how far it arrives, respectively.

Intermittent bursts of strong magnetic activity were described by Sweet *et al.* [56] when they investigated the dynamo action of a 3D chaotic $\boldsymbol{v}$, solution of the MHD equations in three dimensions with periodic boundary conditions. They found that the transition from $\boldsymbol{B} = 0$ to bursts takes place when a Lyapunov exponent becomes positive for perturbations transverse to the invariant manifold $\boldsymbol{B} = 0$, which contained an already chaotic $\boldsymbol{v}$ for parameter values under the critical. However, as far as we know the cyclic generation of bursts of magnetic field has not been reported before in MHD, but bursting and spiking behavior is well known in other fields as nonlinear optics [57], mathematical models of excitable neurons [58], and, in general, in the presence of excitable media [59]. Despite these spikes and trains of spikes are very narrow, they grow exponentially in a very short timescale compared with the time between them.

Although the velocity fields used as dynamo generators were obtained from a thermal convection problem of a pure fluid in spherical geometry, a global dynamics similar to that described here is shared by many other systems in fluid dynamics. For instance, in Ref. [60] the presence of concentration gradients gives rise to heteroclinic chains connecting different objects. Consequently, the global mechanism of generation of $\boldsymbol{B}$ in the form of bursts is probably a general phenomenon due to this dynamics, although the structure of $\boldsymbol{B}$ will change in each problem.

ACKNOWLEDGMENTS

This work has been supported by Spanish MINECO/FEDER under grant FIS2016-76525-P and Catalan AGAUR under grant 2017-SGR-1374. We thank Prof. F. Moreno-Insertis for his useful suggestions on the bibliography.

---

[1] W. Hirsching and F. H. Busse, "Stationary and chaotic dynamos in rotating spherical shells," Phys. Earth Planet. Inter. **90**, 243–254 (1995).

[2] G. A. Glatzmaier and P. H. Roberts, "An anelastic evolutionary geodynamo simulation driven by compositional and thermal convection," Physica D **97**, 81–94 (1996).

[3] E. Grote and F. H. Busse, "Dynamics of convection and dynamos in rotating spherical fluid shells," Fluid Dyn. Res. **28**, 349–356 (2001).

[4] F. H. Busse, "Homogeneous Dynamos in Planetary Cores and in the Laboratory," Ann. Rev. Fluid Mech. **405** (2000).

[5] K. Zhang and G. Schubert, "Magnetohydrodynamics in Rapidly Rotating Spherical Systems," Ann. Rev. Fluid Mech. **32**, 409–443 (2000).

[6] M. H. Heimpel, J. M. Aurnou, F. M. Al-Shamali, and N. Gomez Perez, "A numerical study of dynamo action as a function of spherical shell geometry," Earth Planet. Sc. Lett. **236**, 542–557 (2005).

[7] F. H. Busse and R. Simitev, "Parameter dependences of convection-driven dynamos in rotating spherical shells," Geophys. Astrophys. Fluid Dyn. **100**, 341–361 (2006).

[8] N. Gillet, D. Brito, D. Jault, and H.-C. Nataf, "Experimental and numerical studies of magnetoconvection in a rapidly rotating spherical shell," J. Fluid Mech. **580**, 123–143 (2007).

[9] K. M. Soderlund, E. M. King, and J. M. Aurnou, "The influence of magnetic fields in planetary dynamo models," Earth Planet. Sc. Lett. **333–334**, 9–20 (2012).

[10] F. Feudel, L. S. Tuckerman, M. Zaks, and R. Hollerbach, "Hysteresis of dynamos in rotating spherical shell convection," Phys. Rev. Fluids **2**, 053902 (2017).

[11] K. Hori, R. J. Teed, and C. A. Jones, "The dynamics of magnetic Rossby waves in spherical dynamo simulations: A signature of strong-field dynamos?" Phys. Earth Planet. Inter. **276**, 68–85 (2018).

[12] M. Meneguzzi, U. Frisch, and A. Pouquet, "Helical and Nonhelical Turbulent Dynamos," Phys. Rev. Lett. **47**, 1060–1064 (1981).

[13] R. M. Kinney, B. Chandran, S. Cowley, and J. C. McWilliams, "Magnetic Field Growth and Saturation in Plasmas with Large Magnetic Prandtl Number. I. The Two-dimensional Case," Astrophys. J. **545**, 907–921 (2000).

[14] A. A. Schekochihin, S. C. Cowley, S. F. Taylor, J. L. Maron, and J. C. McWilliams, "Simulations of the Small-Scale Turbulent Dynamo," Astrophys. J. **612**, 276–307 (2004).

[15] F. Cattaneo and S. M. Tobias, "Dynamo properties of the turbulent velocity field of a saturated dynamo," J. Fluid Mech. **621**, 205214 (2009).

[16] A. W. Hood and D. W. Hughes, "Solar magnetic fields," Phys. Earth Planet. Inter. **187**, 78–91 (2011).

[17] A. Brandenburg, "Magnetic Prandtl Number Dependence of the Kinetic-to-Magnetic Dissipation Ratio," Astrophys. J. **791**, 10 (2014).

[18] I. Thaler and H. C. Spruit, "Small-scale dynamos on the solar surface: dependence on magnetic Prandtl number," A&A **578**, A54 (2015).

[19] A. Brandenburg and M. Rempel, "Reversed Dynamo at Small Scales and Large Magnetic Prandtl Number," Astrophys. J. **879**, 9pp (2019).

[20] E. T. Vishniac and J. Cho, "Magnetic Helicity Conservation and Astrophysical Dynamos," Astrophys. J. **550**, 752–760 (2001).

[21] S. Xu and A. Lazarian, "Turbulent Dynamo in a Conducting Fluid and a Partially Ionized Gas," Astrophys. J. **833**, 215 (2016).

[22] A. Brandenburg and K. Subramanian, "Astrophysical magnetic fields and nonlinear dynamo theory," Phys. Rep. **417**, 1–209 (2005).

[23] C. A. Jones, "Planetary Magnetic Fields and Fluid Dynamos," Ann. Rev. Fluid Mech. **43**, 583–614 (2011).

[24] A. S. Brun and M. K. Browning, "Magnetism, dynamo action and the solar-stellar connection," Living Rev. Sol. Phys. **14**, 1–133 (2017).

[25] M. R. E. Proctor and A. D. Gilbert, *Lectures on Solar and Planetary Dynamos*, Isaac Newton Institute for Mathematical Sciences Cambridge: Publications of the Newton Institute (Cambridge University Press, 1994).

[26] S. Molokov, R. Moreau, and H. K. Moffatt, *Magnetohydrodynamics: Historical Evolution and*

Trends, Fluid Mechanics and its Applications, Vol. 80 (Springer, 2007).

[27] E. Dormy and A. M. Soward, eds., *Mathematical Aspects of Natural Dynamos*, The Fluid Mechanics of Astrophysics and Geophysics, Vol. 13 (Chapman & Hall/CRC, 2007).

[28] K. Moffatt and E. Dormy, *Self-Exciting Fluid Dynamos*, Cambridge Texts in Applied Mathematics, Vol. 59 (Cambridge University Press, 2019).

[29] D. Biskamp, *Nonlinear Magnetohydrodynamics*, Cambridge Monographs on Plasma Physics (Cambridge University Press, 1997).

[30] J. Sánchez, F. Garcia, and M. Net, "Critical torsional modes of convection in rotating fluid spheres at high Taylor numbers," J. Fluid Mech. **791** (2016).

[31] K. Zhang, K. Lam, and D. Kong, "Asymptotic theory for torsional convection in rotating fluid spheres," J. Fluid Mech. **813**, R2–1–R2–11 (2017).

[32] D. Kong, K. Zhang, K. Lam, and A. P. Willis, "Axially symmetric and latitudinally propagating nonlinear patterns in rotating spherical convection," Phys. Rev. E **98**, 031101(R) (2018).

[33] G. A. de Wijs, G. Kresse, L. Vočadlo, D. Dobson, D. Alfè, M. J. Gillan, and G. D. Price, "The viscosity of liquid iron at the physical conditions of the Earth's core," Nature **392**, 805–807 (1998).

[34] A. Ribeiro, G. Fabre, J.-L. Guermond, and J. M. Aurnou, "Canonical Models of Geophysical and Astrophysical Flows: Turbulent Convection Experiments in Liquid Metals," Metals **5**, 289–335 (2015).

[35] S. Hanasoge, L. Gizon, and K. R. Sreenivasa, "Seismic Sounding of Convection in the Sun," Ann. Rev. Fluid Mech. **48**, 191–217 (2016).

[36] J. Sánchez Umbría and M. Net, "Torsional solutions of convection in rotating fluid spheres," Phys. Rev. Fluids **4**, 013501 (2019).

[37] M. A. Calkins, L. Long, D. Nieves, K. Julien, and S. M. Tobias, "Convection-driven kinematic dynamos at low Rossby and magnetic Prandtl numbers," Phys. Rev. Fluids **1**, 083701 (2016).

[38] L. K. Currie and S. M. Tobias, "Convection-driven kinematic dynamos with a self- consistent shear flow," Geophys. Astrophys. Fluid Dyn. **113**, 131–148 (2019).

[39] J. R. Gog, I. Oprea, M. R. E. Proctor, and A. M. Rucklidge, "Destabilization by noise of transverse perturbations to heteroclinic cycles: a simple model and an example from dynamo theory," Proc. Roy. Soc. Lond. A **455**, 4205–4222 (1999).

[40] I. Oprea, P. Chossat, and D. Armbruster, "Simulating the Kinematic Dynamo Forced by

Heteroclinic Convective Velocity Fields," Theor. Comput. Fluid Dyn. **9**, 293–309 (1997).

[41] P. Chossat, F. Guyard, and R. Lauterbach, "Generalized Heteroclinic Cycles in Spherically Invariant Systems and Their Perturbations." J. Nonlin. Sci. **9**, 479–524 (1999).

[42] M. L. Dudley and R. W. James, "Time-dependent kinematic dynamos with stationary flows," Proc. Roy. Soc. Lond. A **425** (1989).

[43] K. Li, P. W. Livermore, and A. Jackson, "An optimal Galerkin scheme to solve the kinematic dynamo eigenvalue problem in a full sphere," J. Comput. Phys. **229**, 8666 – 8683 (2010).

[44] R. B. Lehoucq, D. C. Sorensen, and C. Yang, *ARPACK User's Guide: Solution of Large-Scale Eigenvalue Problems with Implicitly Restarted Arnoldi Methods*, Software, Environments, Tools (SIAM, 1998).

[45] J. Sánchez and M. Net, "Numerical continuation methods for large-scale dissipative dynamical systems," Eur. Phys. J. Special Topics **225**, 2465–2486 (2016).

[46] F. Garcia, M. Net, B. García-Archilla, and J. Sánchez, "A comparison of high-order time integrators for the Boussinesq Navier-Stokes equations in rotating spherical shells," J. Comput. Phys. **229**, 7997–8010 (2010).

[47] A. C. Hindmarsh, "ODEPACK, A Systematized Collection of ODE Solvers," in *Scientific Computing*, IMACS Transactions on Scientific Computation, Vol. 1, edited by R. S. Stepleman *et al.* (North-Holland, Amsterdam, 1983) pp. 55–64.

[48] J. P. Boyd, *Chebyshev and Fourier Spectral Methods* (Springer, New York, 1989).

[49] See the Supplemental Material at `http://link.aps.org/supplemental/***` for two animations of the velocity field.

[50] N. L. Peffley, A. B. Cawthorne, and D. P. Lathrop, "Toward a self-generating magnetic dynamo: The role of turbulence," Phys. Rev. E **61**, 5287–5294 (2000).

[51] A. Tilgner, "Onset of dynamo action in an axisymmetric flow," Phys. Rev. E **66**, 017304–1–017304–4 (2002).

[52] M. Landeau and J. Aubert, "Equatorially asymmetric convection inducing a hemispherical magnetic field in rotating spheres and implications for the past martian dynamo," Phys. Earth Planet. Inter. **185**, 61–73 (2011).

[53] W. Herreman and P. Lesaffre, "Stokes drift dynamos," J. Fluid Mech. **679**, 32–57 (2011).

[54] M. Golubitsky, I. Stewart, and D. G. Schaeffer, *Singularities and Groups in Bifurcation Theory*, Vol. II (Springer, New York, 1988).

[55] P. W. Livermore, D. W. Hughes, and S. M. Tobias, "Nonlinear generation of large-scale magnetic fields in forced spherical shell dynamos," Phys. Fluids **22**, 037101 (2010).

[56] D. Sweet, E. Ott, T. M. Antonsen, D. P. Lathrop, and J. M. Finn, "Blowout bifurcations and the onset of magnetic dynamo action," Phys. Plasmas **8**, 1944–1952 (2001).

[57] J. G. Freire, R. Meucci, F. T. Arecchi, and J. A. C. Gallas, "Self-organization of pulsing and bursting in a CO_2 laser with opto-electronic feedback," Chaos **25**, 097607 (2015).

[58] P. Channell, G. Cymbalyuk, and A. Shilnikov, "Origin of bursting through homoclinic spike adding in a neuron model," Phys. Rev. Lett. **98**, 134101 (2007).

[59] M. Desroches, J. Guckenheimer, B. Krauskopf, C. Kuehn, H. Osinga, and M. Wechselberger, "Mixed-mode oscillations with multiple time scales," SIAM Rev. **54**, 211–288 (2012).

[60] O. Batiste, E. Knobloch, I. Mercader, and M. Net, "Simulations of oscillatory binary fluid convection in large aspect ratio containers," Phys. Rev. E **65**, 016303(1–19) (2002).